SRON
Netherlands Institute for Space Research

Faculteit Bètawetenschappen

Utrecht University

Bachelor thesis

Exploration of Fermi GBM TTE data

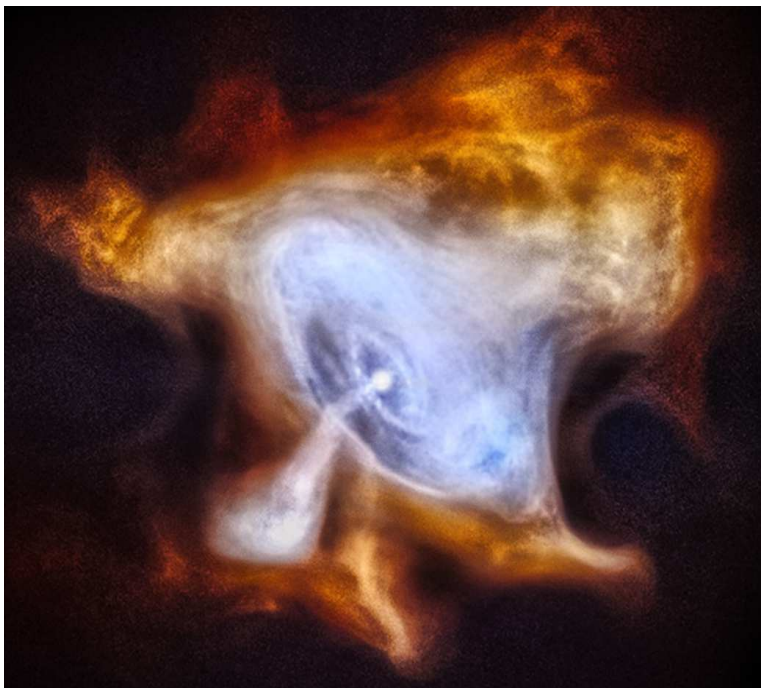

Author:
Jaylesh Darshan Soebedar
Student number: 3995461
Utrecht University
Study: Physics & Astronomy

Supervisors:
Dr. Lucien Kuiper
SRON
and
Prof. Dr. Christiane de Morais Smith
Utrecht University

15 June 2016

Abstract

During this bachelor research I did an exploration of Fermi GBM TTE data in studying energetic fast pulsars. The Fermi Gamma-ray Burst Monitor (GBM) operates in a new default data taking mode since 26 November 2012. In this mode events are time-tagged with a 2 μs precision for 128 different energy channels in the 8 keV-30 MeV regime. Data from this mode is used to analyse the pulsars PSR B0531+21 (the Crab pulsar), PSR B1509-58 and 1RXS J170849.0-400910 with spin periods of approximately 33 ms, 150 ms and 11 s, respectively. The 2 μs precision provides for each of the three pulsars a more than sufficient time resolution. However, since this was not required for the pulsars PSR B1509-58 and 1RXS J170849.0-400910 I reduced the sampling time to enhance the computation speed.
Based on this work I conclude that Fermi GBM TTE data can be used to produce pulse profiles, which show clear resemblance with profiles from earlier observations by other high-energy instruments, for all three pulsars.
I produced phase folded pulse profiles for PSR B0531+21 with significances well above 36σ analysing 0.42 Ms exposure time per detector, and for PSR B1509-58 significances $\sim 36.0\sigma$ analysing 15.66 Ms exposure time per detector.
Although I was able to produce phase folded pulse profiles for 1RXS J170849.0-400910 the data consist of unexpectedly strong signals for certain time intervals. More research has to be done to find the origin of this. These signals are likely caused by erratic strong flares of high-mass X-ray binary 4U1700-377 which is located at only 3° from 1RXS J170849.0-400910 and thus always in the selected data sample.

Key words: gamma rays: observations: Fermi GBM TTE: pulsars: PSR B0531+21: PSR B1509-58: 1RXS J170849.0-400910

On the title page the Crab nebula is shown in X-ray. Shown in red, green and blue are the $0.5-1.2$, $1.2-2.0$ and $2.0-7.0$ keV energy bands, respectively [Footnote 2].

Contents

Chapter 1

Introduction

In this work I analysed data on various fast spinning neutron stars, or pulsars. Neutron stars are very dense objects that form at the end of the stellar evolution of high mass stars. It is still unknown what the interior of neutron stars consist of as the interior density is higher than the nuclear density. Observing pulsars can thus help understanding the nuclear force.
The high mass of neutron stars also suggest that they produce gravitational waves when found in binary systems. Timing analysis of pulsars in binary systems can provide information which can be used to investigate general relativistic properties.
In this work I used the symbol $\odot$ to indicate the Sun i.e. $M_\odot$ indicates the solar mass, $R_\odot$ the solar radius and $L_\odot$ the solar luminosity.

1.1 Stellar evolution

At the end stage of stellar evolution stars collapse when the gravitational force exceeds the outwards pressure. This pressure can be due to thermal pressure or, as in the case of the dense objects discussed below, mainly due to degeneracy pressure.
Due to conservation of angular momentum and magnetic flux in the core the dense objects often have high rotation periods and magnetic fields.

1.1.1 White dwarfs

The majority of the stars in the Universe are main sequence stars. These stars have a mass M of several $M_\odot$. After it consumed the Hydrogen in the core to fuse into Helium the stars converts its gravitational energy into thermal energy as the Helium core contracts. The Hydrogen in higher shells then start to fuse into Helium which causes the outer layers of the star to increase in temperature and pressure. The increase in pressure causes the stars radius to increase from $\sim 1.6R_\odot$ to $\sim 170R_\odot$, with a luminosity increase from $\sim 2.2L_\odot$ to $\sim 2300L_\odot$. The red color and size of the star in this phase gives rise to the name "Red Giant".
During the red giant phase the Helium core grows causing the pressure to reach a point where the electrons become degenerate. The degenerate electrons produce a pressure independent of the temperature as the Helium core reaches a temperature of $T \sim 10^8$K. Now the Helium core can start to fuse into Carbon releasing more energy into the core. As the rise in temperature speeds up the fusion process this leads to a runaway fusion until the temperature rises to $T \approx 3.5 \times 10^8$ K. At this temperature the electrons become non-degenerate and the star settles down.
After the Helium in the core is fused into Carbon (this takes approximately 100×10^6 years) the core contracts again and starts a second red giant phase with luminosity $\sim 3000L_\odot$ and varying radius while blowing away its outer layers. As this brief second red giant phase ends only the core is left. This core is called a white dwarf.
Its mass is typically of the order of $M_\odot$ while the radius is of order R_{Earth}, resulting in a very dense object ($\rho \sim 2 \times 10^6 \rho_\odot$) [17].

1.1.2 Neutron stars

When a star of initial mass ($\sim 7M_\odot < M \lesssim 18M_\odot$) [17](p.424) becomes a red giant it has an Iron core with shells fusing different elements around it. When the core exceeds the Chandrasekhar mass $M_{\text{Chandrasekhar}}(\sim 1.44M_\odot)$ the core can not be supported due to electron degeneracy anymore and it will collapse leading to a type II supernova [17]. The resulting core is a neutron star of mass between $M_{\text{Chandrasekhar}}$ and $(2-3)M_\odot$, with a radius in the order of $r \sim$ (5-10) km [16]. Neutron stars can have an interior density $\rho \sim 10 \times \rho_0$, where $\rho_0 \approx 2.8 \times 10^{17}$ kg m^{-3} the nuclear density [4].

1.1.3 Black holes

If the initial mass of the star is larger than $\sim 18M_\odot$ the core will collapse into a black hole. An initial stellar mass of $\sim 18M_\odot$ corresponds to a core of mass $M \gtrsim 3M_\odot$[17](p.424) after collapse, which is the limit for which neutron degeneracy pressure can support the core from collapsing. Black holes are thus the most massive objects that a star can form into after core collapse.
Black holes can be defined as objects whose escape speed is higher than the speed of light c. The Schwarzschild radius of the black hole $r = \frac{2GM}{c^2}$ is the radius inside which nothing can escape the gravitational pull of the object.
If the black hole has a mass $M \approx M_\odot$, the resulting Schwarzschild radius approximately 3 km.

The exact mass limits for white dwarfs and neutron stars depends on the spin of the progenitor star since centrifugal forces counteract the collapse.

1.2 Neutron star classification

First discovered in 1967 during a search for quasars, astronomers at Cambridge thought that the repeating radio signals they observed were due to human, or even extra-terrestrial, activity. Afterwards it turned out that the radio signals kept in pace with the sidereal time and thus were of celestial origin, and the object was called a pulsar. The pulsar had a pulse period of 1.337 s and a pulse duration of ≈ 20 ms, and this led to the notification that pulsars are rotating neutron stars [16].

Observations of pulsars across time scales of months make the measurement of the pulse period P and pulse period derivative $\dot{P}$ possible.
Since the first discovery of a pulsar in 1967 about 2000 more pulsars have been detected. Most pulsars show a $\dot{P} > 0$, indicating a slow-down and that the pulsar loses rotational energy according to equation 1.2.1.

$$\dot{E} = I\Omega\dot{\Omega} = -I\frac{\dot{P}}{P^3} \tag{1.2.1}$$

Where $\dot{E}$ is the time derivative of the energy E, I the moment of inertia and $\Omega = \frac{2\pi}{P}$ the angular frequency. We speak of rotation-powered pulsars [1].

Assuming that the pulsar loses this energy in the form of electromagnetic dipole radiation we obtain two relations between P, $\dot{P}$ and surface magnetic dipole strength B and maximum characteristic age τ, see equations 1.2.2.

$$B_{\text{min}} = 3.3 \times 10^{19}(P\dot{P})^2 \tag{1.2.2a}$$

$$\tau = \frac{P}{2\dot{P}} \tag{1.2.2b}$$

By sorting the P and $\dot{P}$ of these pulsars in a so-called P-$\dot{P}$ diagram (See Fig. 1.1) interesting population properties are revealed, especially when lines of constant magnetic field strength B and age τ are superposed.

The large majority of the rotation-powered pulsars (shown in black in Fig. 1.1) reside in the so-called common cloud with an age between 10 kyr and 100 Myr and magnetic field strengths between $10^{11} - 10^{13}$ Gauss (See middle part of Fig. 1.1).

In the lower left part of Fig. 1.1 the subset of millisecond pulsars shows up with periods between ∼1.5-30 ms and large ages (= old population). Most of these pulsars reside in binary systems, in which the companion star has provided mass and angular momentum through accretion, spinning the pulsar up ($\dot{P} < 0$). The progenitors of this class of millisecond pulsars are accretion-powered (millisecond) pulsars in which mass transfer powers the systems (potential energy).

Finally, in the top right part the so-called magnetar population pops up, there are currently $\sim$ 20 known (part of which are shown in red in Fig. 1.1).
These pulsars are slowly rotating neutron stars with magnetic fields well above the 'critical' quantum limit of $B_{\rm crit}$, see equation 1.2.3.
These systems are powered by the decay of strong internal magnetic fields of order of $\sim 10^{15} - 10^{16}$ Gauss (=magnetically powered).

$$B_{\rm crit} = \frac{m_e c^3}{e\hbar} = 4.413 \times 10^{13} [\text{Gauss}] \tag{1.2.3}$$

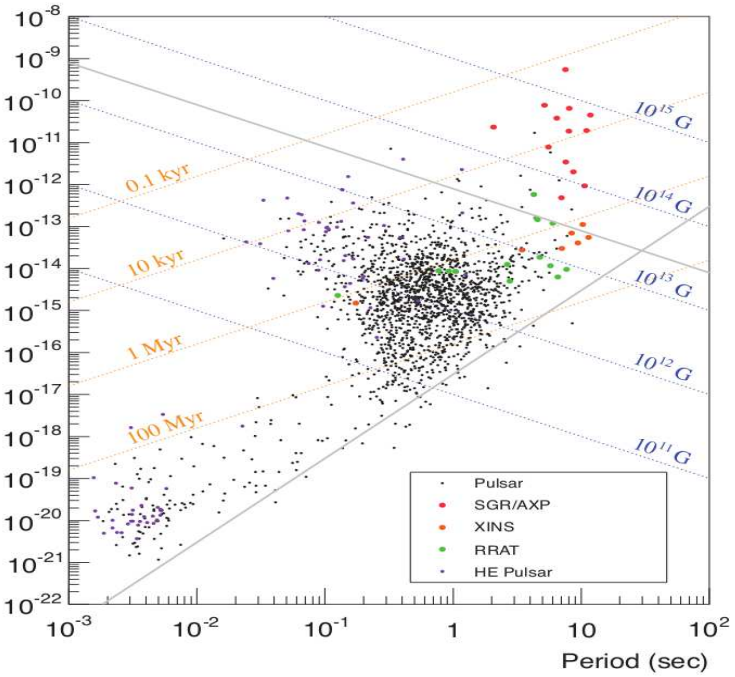

Figure 1.1 – A P-$\dot{P}$ diagram showing the majority of known pulsars. Lines of constant dipole magnetic field strength and maximum pulsar age are indicated as dotted blue and yellow lines, respectively. The black dots show rotation-powered pulsars and red dots show magnetars. The y-axis shows the unitless period derivative $\dot{P}$ [9].

Although it is still not exactly known what the interior of neutron stars consist of, there are suggestions of an interior region consisting of superconducting super fluid material [13]. This theory is supported by the observation of glitches.

Glitches are events that cause sudden changes in rotation period. It is thought to be caused by stellar quakes, sudden adjustments of the neutron star's interior that influence the magnetic field.

Anomalous X-ray Pulsars (AXP's) are a type of magnetars that exhibit high X-ray luminosities of several orders of magnitude larger than observed for rotation-powered pulsars [1].
As an example, Fig. 1.2 shows supernova remnant Kes 73 with AXP 1E 1841-045 at its center.

Figure 1.2 – A composite image of the supernova remnant Kes 73 with AXP 1E 1841-045 at its center. Shown in blue, white, orange and red are the X-ray, optical, infrared and radio emissions respectively, as observed by various high-energy instruments [1].

1.3 Pulsars sample to study

During this work I analysed three established high-energy pulsars with widely diverse periods, in the range 10-100 ms (Crab pulsar), 100-1000 ms (PSR 1509-58) and 10-100 s (1RXS J170849.0-400910). Since these three pulsars are active in different time regimes they are suitable for Fermi GBM TTE data exploration (with intrinsic time resolution of 2 μs).

- The first pulsar I analysed is the well-known rotation-powered pulsar PSR B0531+21, more commonly known as the Crab pulsar. This rotation-powered pulsar has a period P_{Crab} of about 33 ms and is located in the center of the pulsar wind nebula called the Crab Nebula (see Fig. 1.3a). This nebula formed after the supernova SN 1054 occurred on 4 July 1054. Since the pulsar is well-known and observed by many instruments it can be used as calibration source.
  Previous observations at high energies ($\gtrsim$ 0.1 keV) of the Crab pulsar show two pulses separated 0.4 phase from each other. The relative height of the two pulses changes as seen in different energy bands. This morphology is clearly visible in the eight panels of Fig. 1.3b.

- The pulsar PSR B1509-58 is located at a distance of about 1700 light years from Earth in the center of the pulsar wind nebula nicknamed "Hand of God" (see Fig. 1.4a). This rotation-powered pulsar has a period P_{1509} of approximately 150 ms.

[1] X-ray, Optical, Radio & Infrared Images of Kes 73. Credit: X-ray: NASA/CXC/Univ. of Manitoba/H.Kumar et al, Optical: DSS, Infrared: NASA/JPL-Caltech, Radio: NSF/NRAO/VLA. URL: http://chandra.si.edu/photo/2014/archives/more.html

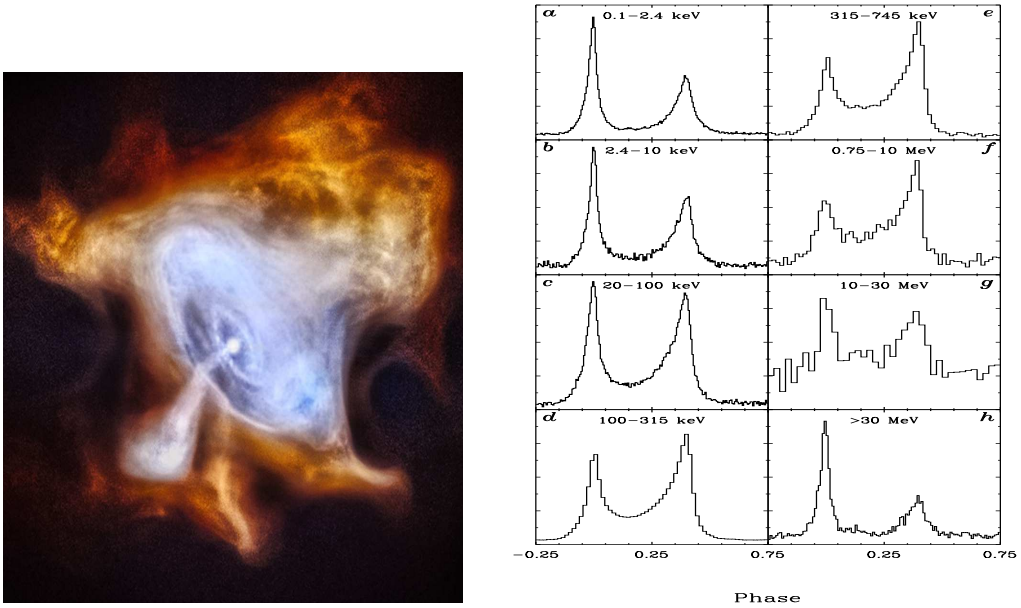

(a) **(b)**

Figure 1.3 – The left figure shows an image of the Crab nebula in X-ray. Shown in red, green and blue are the $0.5-1.2, 1.2-2.0$ and $2.0-7.0$ keV energy bands respectively.[2] The right figure shows pulse profiles of the Crab pulsar in energy bands ranging from 0.1 keV to over 30 MeV, taken by various instruments (a: ROSAT HRI, b: BeppoSAX MECS, c: BeppoSAX PDS, d: CGRO BATSE, e&f: CGRO COMPTEL, h: CGRO EGRET) [12].

It was discovered in data from 1979-1980 in the energy band 0.2-4 keV. Ever since then numerous observations have been performed in different energy bands. Figure 1.4b shows pulse profiles (i.e. pulse phase distributions) in the energy bands from 2 keV to over 1 GeV with two cycli shown (Kuiper & Hermsen. 2015)[10]. The pulse profile shows a peak near phase 0.27 (the radio pulse arrives at phase 0) [11].

- The AXP 1RXS J170849.0-400910 is located 15° from the galactic center as seen from the Earth. It has a pulse period P_{1708} of about 11s and thus is the slowest pulsar analysed in this research. It was discovered in 1996, with its first glitch, a sudden discontinuity in rotation behavior, detected in 1999. It shows frequent glitches.

The high-energy pulse profiles are shown in Fig. 1.5 (P.R.den Hartog et al., 2008)[6]. Figure 1.5a (left panel) shows the pulse profile as produced by summing all pulse profiles from the panels E-H of the right panel. It shows two cycli where the three colors indicate three phase intervals. The green part indicates the DC level, blue indicates what appears to be a weak pulse with a maximum at approximately 0.475 phase and purple indicates the pulse peak with a maximum near phase 0.8.
Figure 1.5b (right panel) shows the morphology of the pulse profiles for various energy bands. It can be seen clearly that the pulse profile morphology changes drastically for various energy bands [6].

[2] X-ray image of the Crab nebula. Credit: NASA/CXC/SAO. Published in 2014. URL: http://chandra.harvard.edu/photo/2014/15year/

[3] High-Energy X-ray View of 'Hand of God' published by NASA in 2015. Image credits: NASA/JPL-Caltech/McGill URL: http://www.nasa.gov/jpl/nustar/B1509-pia17566

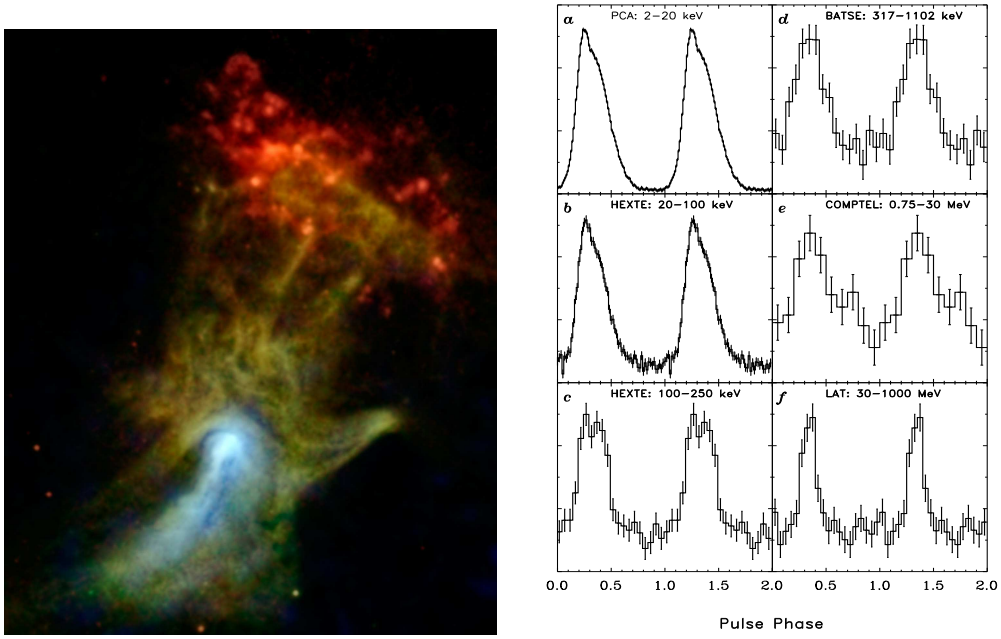

(a) **(b)**

Figure 1.4 – In the left figure, the 'Hand of God' nebula is shown in X-ray. Shown red, green and blue are the 0.5-2, 2-4 and 7-25 keV energy bands respectively. The 0.5-2 keV and 2-4 keV bands are seen by Chandra and the 7-25 keV band by NuSTAR .[3] In the right figure the pulse profiles of the pulsar PSR B1509-58 with energy bands ranging from 2 keV to over 1000 MeV with two cycli as observed by different high-energy instruments are shown [10].

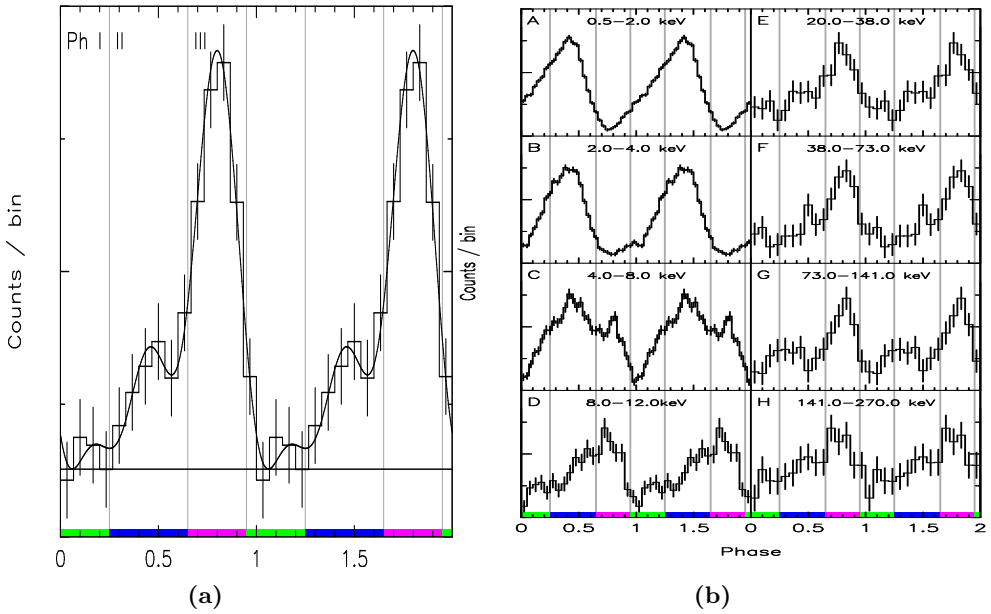

(a) **(b)**

Figure 1.5 – The left panel shows the pulse profiles of AXP 1RXS J170849.0-400910 in energy band 20-270 keV by summing panels E-H of the right panel. The right panel shows the pulse profiles of AXP 1RXS J170849.0-400910 in energy bands between 0.5-270.0 keV. For panels A-D XMM-Newton data is used, for panels E-H ISGRI data is used [6].

Chapter 2

Instrumentation and observed data analysis

2.1 The Fermi Gamma-ray Space Telescope

The Fermi spacecraft, launched on 11 June 2008, contains two instruments, namely the Large Area Telescope (LAT) and the Gamma-ray Burst Monitor (GBM). It orbits the Earth at $\sim$ 565 km altitude at 25.6° inclination with a period of 95.5 minutes.
The LAT is a wide-field telescope sensitive in the $\sim$20 MeV - 300 GeV energy band. The GBM is a gamma-ray detector and consist of several scintillators, the twelve sodium iodide (NaI) scintillators are sensitive in the energy range 8 keV- 1 MeV, and the two bismuth germanate (BGO) scintillators in the energy range 150 keV - 30 MeV, thus overlapping with the energy range of the LAT. The left part of Fig. 2.1 shows the spacecraft during its assemblance: the LAT at the top part covered with reflective material, and in front 6 NaI detectors and 1 BGO detector of the GBM. Figure 2.1 shows on the right a schematic view of the GBM and the used Fermi spacecraft coordinate system [8].

Since 26 November 2012 the GBM is operating in a nominal operating mode in which it registers time-tagged events (TTE) with a precision of 2 μs in 128 energy channels for every detector. The GBM time is synchronized to GPS once per second [2]. Thus, this offers the opportunity to study for the first time systematically fast pulsars emitting high-energy radiation.

In this work I used the twelve NaI scintillators. The angles in which the NaI detector pointings are oriented with respect to the Fermi spacecraft coordinate system are shown in table 2.1.

2.1.1 Data screening

- Some charged particles from the solar winds and cosmic rays can get trapped due to the Earth's magnetic field. Since the magnetic field of the Earth is not symmetric the charged particles get trapped at different distances from the Earth's surface, ranging from approximately $(1.2 - 1.3) \times 10^3$ km on one side of the Earth to $(2 - 8) \times 10^2$ km on the other side. This region is called the Van Allen belt.
  The lower side of the Van Allen belt is located above the region between South-America, Africa and Antarctica and is called the South Atlantic Anomaly (SAA) [5].

  When the Fermi Gamma-ray Space Telescope passed through the SAA the instruments are turned off. In data analysis I extended this for approximately 600 s on both sides to remove data still showing signs of high activation.

- The Earth is a strong source of high-energy radiation, X-rays and γ-rays, mainly originating from interaction between high-energy particles from the solar wind and

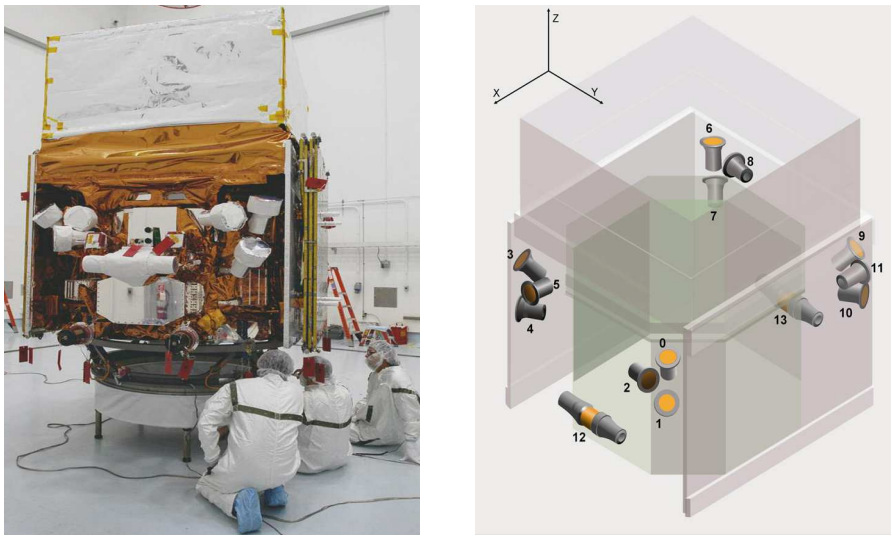

Figure 2.1 – Left: A picture taken while assembling the Fermi spacecraft, where some Fermi GBM detectors can be seen. Right: A schematic view of the Fermi GBM detectors, with the Fermi spacecraft coordinates as indicated [14].

Table 2.1 – Orientation of NaI detector pointings with respect to Fermi spacecraft coordinates [14].

Detector ID number	Azimuth (Deg)	Zenith(Deg)
0	45.9	20.6
1	45.1	45.3
2	58.4	90.2
3	314.9	45.2
4	303.2	90.3
5	3.5	89.8
6	224.9	20.4
7	224.6	46.2
8	236.6	90.0
9	135.2	45.6
10	123.7	90.4
11	183.7	90.3

cosmic rays. Therefore, I restricted ourselves to data collection, while the angle between the Earth zenith and the detector pointing was less than 128°, significantly cutting out the Earth's contributions. The angle of 128° is used since it yielded to the best signal-to-noise ratio for X-ray binary Her X-1 (used as calibration source) [1].

- The NaI detectors hardly have any directional response. I selected data only when the angle between the detector pointing and the source is less than 58°, this corresponds to maximum signal-to-noise ratio for Her X-1 [1]).

2.2 Timing analysis

2.2.1 Barycentering

To describe fast periodic phenomena across long timescales, I need a proper reference frame.
The 'best' conceivable frame is an inertial frame with its origin at the Solar-System barycenter. Therefore, arrival times registered at an Earth orbiting spacecraft have to be converted to arrival times at the Solar-System Barycenter (SSB). This involves

the calculation of travel time delays and some time dependent relativistic effects (e.g. Earth/spacecraft moving through time-dependent solar-system potential field yielding time depending gravitational red-shifts). This process is called 'barycentering'.
Necessary components to perform this are:

- The source location on the sky of the pulsar.
- The JPL Solar System ephemeris DE200, which provides position and velocities of the Sun, Earth, Moon, other planets and major asteroids as function of time.
- The instantaneous spacecraft position with respect to Earth's center.

For the Fermi GBM data the barycentric corrections are performed in IDL tools developed by my supervisor Dr. L. Kuiper.

2.2.2 Timing models

Timing models, or ephemerides provide information about the rotation behavior of the pulsar. It contains the spin frequency ν ($=\frac{1}{P}$) and its first two time derivatives $\dot{\nu}$ and $\ddot{\nu}$ valid at epoch time t_0 across a certain time validity interval. Every rotation of the pulsar can be accurately accounted for!
These models are used to calculate the pulse phase of events for which the arrival times are barycentered.

Converting the time of arrival to the phase of the events is done by using equation 2.2.1. Here is t_0 the reference time, ϕ_0 the phase on t_0 and $\Delta t = t_{\mathrm{BTOV}} - t_0$ the difference between the barycentered time of arrival t_{BTOV} and t_0.
The used timing models are shown in table 2.2 for each pulsar. Times are indicated here in Modified Julian Day (MJD), which corresponds to the number of days passed since 17 November 1858 at 00:00 and this is used frequently by astronomers to indicate times.

$$\phi = \nu\Delta t + \frac{1}{2}\dot{\nu}\Delta t^2 + \frac{1}{6}\ddot{\nu}\Delta t^3 + \phi_0 \tag{2.2.1}$$

After calculating the phase of each event, the obtained phases are put in a histogram, resulting in a pulse phase distribution, or pulse profile. In this work I showed one $\sigma = \sqrt{N}$ error bars in the pulse profiles, where N represents the number of events in the pulse profile. (See Fig. 3.1 as an example.)

Table 2.2 – Time models used in this study

Source	t MJD	t_0 MJD	ν Hz	$\dot{\nu}$ $\times 10^{-11}$Hz/s	$\ddot{\nu}$ $\times 10^{-22}$Hz/s^2
PSR B0531+21	55464-55548	55464	29.7198319307843	-37.1141	0.926
PSR B1509-58	56670-57081	55393	6.5967641614772	-6.65195	1.88
PSR B1509-58	56670-57081	56876	6.5882563984560	-6.62783	19.4
PSR B1509-58	57013-57372	57191	6.5864475496980	-6.62267	18.9
1RXS J1708-40	56155-56483	56155	0.0908490940608	-0.0162426	0.00
1RXS J1708-40	56591-56797	56686	0.0908415914927	-0.0165385	0.00
1RXS J1708-40	56591-57133	56591	0.0908429514768	-0.0166198	1.02
1RXS J1708-40	56591-57133	56591	0.0908429514768	-0.0166198	1.02
1RXS J1708-40	57111-57322	57111	0.0908355861132	-0.0164703	0.00

2.3 Analysis of pulse-phase distributions

To analyse the pulse profiles I used Z_n^2-statistics. Here Z_n^2 is defined in equation 2.3.1, where N again represents the number of events in the pulse profile and n the n^{th} harmonic. It evolves as a χ^2_{2n} probability density function for $N \to \infty$.

The Z_n^2-statistics provides a measure for the signal-to-noise ratio, the higher the value of Z_n^2 for a given n, the higher the signal-to-noise ratio, in this work it is expressed in Gaussian sigma's [3].

$$Z_n^2 = \frac{2}{N} \sum_{k=1}^{n} \left((\sum_{j=1}^{N} \cos\, k\phi_j)^2 + (\sum_{j=1}^{N} \sin\, k\phi_j)^2 \right) \tag{2.3.1}$$

Chapter 3

Results and discussion

3.1 The Crab Pulsar

As the Crab pulsar has a period of $P_{\text{Crab}} \approx 33$ ms I used the intrinsic time resolution of 2μs for the data analysis.

The TTE data used were collected by FERMI GBM during mission weeks 375-378 from 06-08-2015(=57240 MJD) to 02-09-2015(=57267 MJD). The data yielded after applying our screening criteria an average exposure of 0.42 Ms per NaI detector. After phase folding these four weeks of data I constructed the pulse profiles shown in Fig. 3.1.
The Z_9^2-test significance is over 36σ for all panels shown except for the panel in the lower right corner showing the pulse profile for 300-750 keV. There the Z_9^2-test significance is equal to approximately 10.6σ. Here I used the harmonic $n = 9$ since the pulse profile is sharp [3].

Figure 3.1 shows two cycli where one of the peaks is located near phase 1.0, and another at phase ~ 0.4, consistent with (Kuiper et al., 2001) [12].
The same change in profile morphology, as function of energy shown in Fig. 1.3b, is visible in our pulse profiles, where only four weeks of Fermi GBM TTE data is used. This demonstrates the great potential of GBM TTE data to study fast pulsars (even millisecond pulsars).

3.2 PSR B1509-58

Since the pulsar PSR B1509-58 has a rotation period of $P_{1509} \approx 150$ ms I experimented with the time sampling by setting it to the intrinsic time resolution of 2 μs, 5 ms and 10 ms for different time segments in order to follow the structure in the folded light curves at sufficient accuracy.

The data used for this bachelor's project were collected by FERMI GBM during mission weeks 235-393 from 29-11-2012 (=56260 MJD) to 17-12-2015 (=57373 MJD). These 159 weeks of data yielded, after applying our screening criteria, an average exposure of 15.66 Ms per NaI detector.

The first 17 weeks of data were analysed using the intrinsic time resolution of 2 μs. A typical run analysing 1 week of data took about 60 hours processing time, mainly caused by the event-by-event barycentering process of the huge input event files.

To speed up processing time I introduced a sampling time of 5 ms, amply sufficient to cover the 150 ms pulse profile of PSRB1509-58, for the next 91 weeks. This yielded an enormous gain in processing speed: analysing 1 week data took about 8 hours processing time.

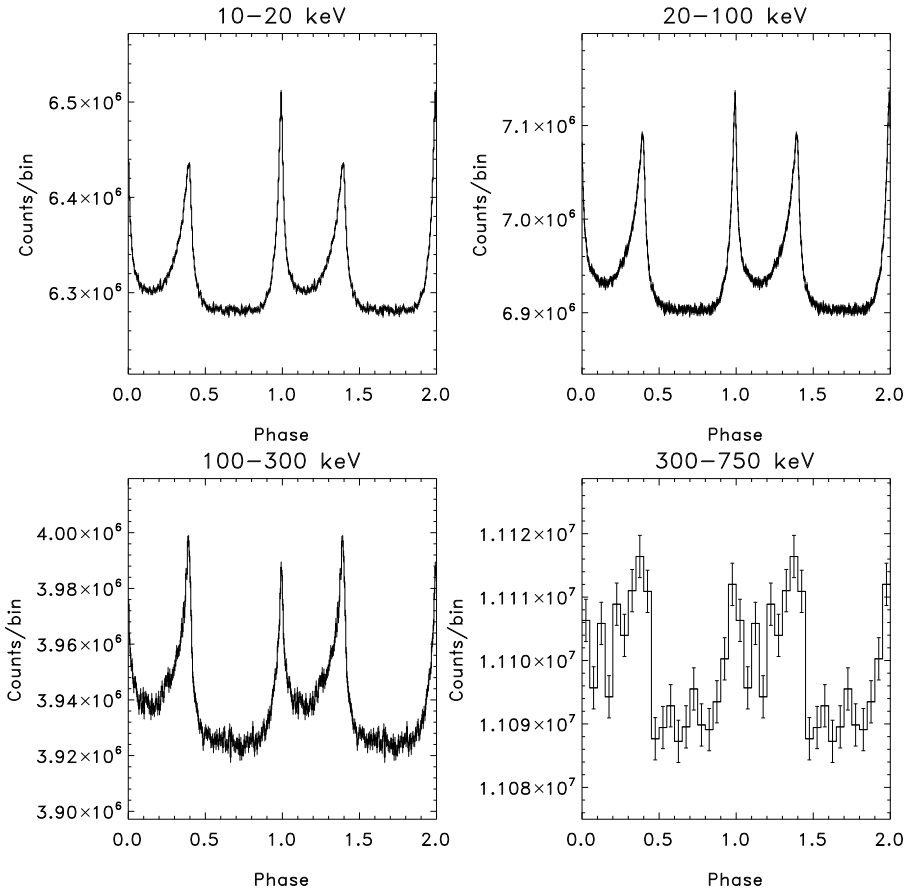

Figure 3.1 – Pulse profiles of the Crab pulsar in energy bands from 10 keV to 750 keV produced using Fermi GBM TTE data, with 1 σ error bars indicated. Two cycli are shown for clarity.

Finally, the last 51 weeks are analysed applying a 10 ms sampling time, increasing the speed to about 6 hours per week processing time.

The resulting pulse phase distributions for the combination of the 17, 91 and 51 weeks, are shown for four different energy bands in Fig. 3.2. The Z_2^2-test significances are 22.9σ, 36.0σ, 34.0σ and 8.4σ for the upper left (10-20 keV), right (20-100 keV) and bottom left (100-300 keV) and right (300-750 keV) panels, respectively.

Comparison of Fig. 3.2 with panels a (2-20 keV), b (20-100 keV), c (100-250 keV) and d (317-1102 keV) of Fig. 1.4b show strong similarities, with the asymmetric pulse near phase ∼0.27.
It also demonstrates that the Fermi GBM TTE data yielded a significantly better pulse profile in the 100-300 keV energy band than the previous best RXTE HEXTE one for the 100-250 keV band.

3.3 1RXS J170849.0-400910

The AXP 1RXSJ170849.0-400910 has a rotation period of about ∼ 11 s, and thus a time sampling of 50 ms is amply sufficient to cover the pulse-profile.

I analysed data from Fermi mission weeks 235-266 and 282-386 (MJD 56260-57323; 29-11-2012 - 28-10-2015). The data gap for weeks 267-281 is caused by the loss of phase-

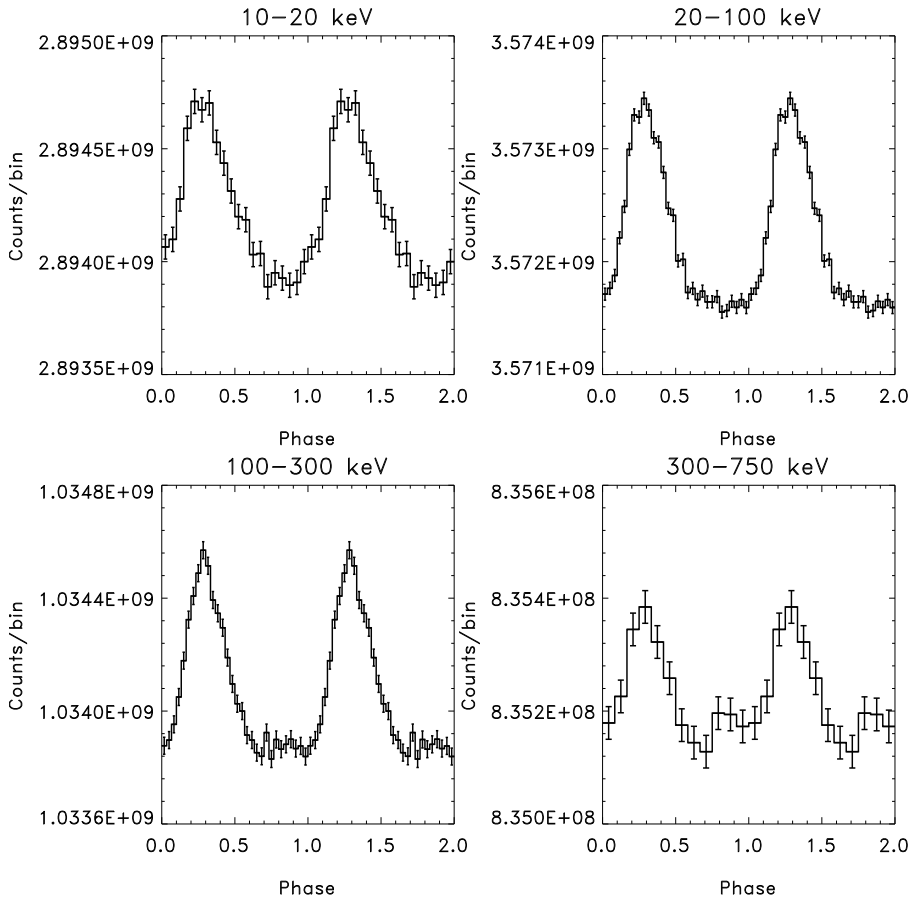

Figure 3.2 – Pulse profiles of the pulsar PSR B1509-58 in energy bands from 10 keV to 750 keV produced using Fermi GBM TTE data, with 1 σ error bars indicated. Two cycli are shown for clarity.

coherence during this period, and thus no valid timing model is available covering this time interval.

The average exposure time per NaI detector amounts 14.06 Ms.

Pulse profiles for the energy bands 20-100, 100-300 and 20-300 keV, after phase folding TTE event data from the combination of all weeks, are shown in Fig. 3.3.
The corresponding Z_2^2-test significances for the 20-100, 100-300 and 20-300 keV bands are 12.2σ, 9.0σ and 14.7σ, respectively.

If we compare these Fermi GBM results with previous findings, (den Hartog et al., 2008) (see Fig. 1.5), we notice differences in morphology, especially below 100 keV, The Fermi GBM profiles look broader. And the obtained Z_2^2-test significances are higher than expected.

Therefore, I break-down the full GBM data set in several parts, combining different mission weeks.
Comparing the profiles from these subsets yielded inconsistent results, in particular the morphologies and significances of various pulse-phase distributions for the same energy band vary dramatically. Instead I expected a 'steady' build-up of the signal.

The apparent time variability is very likely not intrinsic to 1RXS J170849.0-400910 and its cause is very likely related to rapid strong flux variations of nearby sources in the GBM field-of-view.

A potential candidate is high-mass eclipsing X-ray binary 4U 1700-377 at only $\sim 3°$ from 1RXS J170849.0-400910 (and thus is always included in the selected GBM data sample).

It is known that this source shows bright flares, reaching flux levels up to a couple of times the Crab flux, for periods that can last several hours [15].

A way to prove, that 4U 1700-377 is responsible for the time variable morphology and high Z_n^2-test significance of the 1RXS J170849.0-400910 profiles, is to select only time periods for the GBM analysis, when 4U 1700-377 is in eclipse (about for 20% of the time) [7].

During this period I expect a 'normal' signal build-up because of the absence of the disturbing presence of high-energy emission from 4U 1700-377.

However, this work is outside the scope of this bachelor's project.

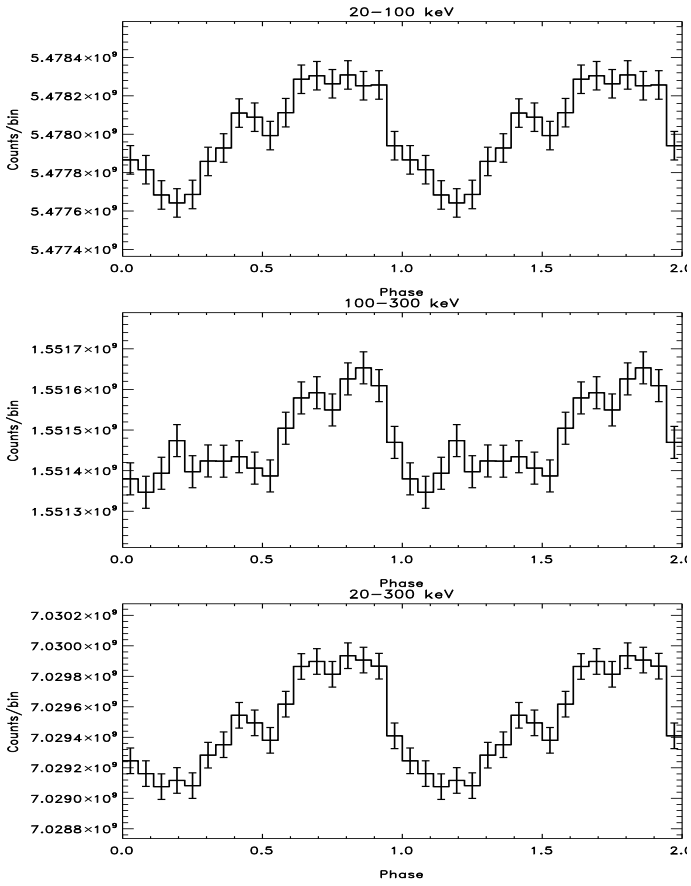

Figure 3.3 – Pulse profiles of the pulsar 1RXS J170849.0-400910 in energy bands from 20 keV to 300 keV produced using Fermi GBM TTE data, with 1 σ error bars indicated. Two cycli are shown for clarity.

Chapter 4

Summary and conclusion

Using Fermi GBM TTE data I analysed the rotation-powered pulsars PSR B0531+21 (also known as the Crab pulsar), PSR B1509-58 and AXP 1RXS J170849.0-400910 with pulse periods covering different time regimes ranging from 33 ms up to 11 s. I demonstrated that Fermi GBM TTE data can be used to accurately derive the pulse-shapes (in absolute phase) for rapidly ($P \lesssim 1$ s) rotating neutron stars for energies in the $\sim$ 10 keV- 1 MeV range, provided that accurate timing models are available.

However, though we clearly detected the pulsed fingerprint of 11 s AXP 1RXS J170849.0-400910 in Fermi GBM TTE data up to $\sim$ 300 keV, we should be cautious in the interpretation with pulsed signals in the 10-100/1000 s regime because interference with strong flaring nearby field-of-view sources can occur.
The latter cases require in-depth detail studies.

Acknowledgements

I had a very pleasant time at SRON. I would therefore like to thank the Netherlands Institute for Space Research (SRON) for the opportunity to do my bachelor research at their department in Utrecht and for the opportunity to visit the Nederlandse Astronomen Conferentie (NAC), showing me a broad range of research subjects within astrophysics which inspires me to continue the study in astrophysics.
I would also like to thank the SRON astrophysics group for the nice time and many laughs during the SRON coffee breaks and the NAC. I would like to thank Dr. C. de Morais Smith for being my official supervisor at Utrecht University.
And I would especially like to express my gratitude to Dr. L. Kuiper for his time and supervision during this entire project.

Bibliography

[1] Felix ter Beek. "FERMI GBM detections of four AXPs at soft gamma-rays". Supervisor: Prof. dr. W. Hermsen, Daily Supervisor: Dr. L. Kuiper. MA thesis. University of Amsterdam, Nov. 2012.

[2] N. Bhat. *Fermi GBM instrument*. URL: http://f64.nsstc.nasa.gov/gbm/ (visited on 06/13/2016).

[3] R Buccheri et al. "Search for pulsed gamma-ray emission from radio pulsars in the COS-B data". In: *Astronomy and Astrophysics* 128 (1983), pp. 245–251.

[4] Nicolas Chamel et al. "On the maximum mass of neutron stars". In: *International journal of modern physics E* 22.07 (2013), p. 1330018.

[5] Imke De Pater and Jack J Lissauer. *Planetary sciences*. Cambridge University Press, 2015.

[6] PR Den Hartog, L Kuiper, and W Hermsen. "Detailed high-energy characteristics of AXP 1RXS J170849-400910-Probing the magnetosphere using INTEGRAL, RXTE, and XMM-Newton". In: *Astronomy & Astrophysics* 489.1 (2008), pp. 263–279.

[7] M Falanga et al. "Ephemeris, orbital decay, and masses of ten eclipsing high-mass X-ray binaries". In: *Astronomy & Astrophysics* 577 (2015), A130.

[8] *GBM Data Products*. URL: http://fermi.gsfc.nasa.gov/ssc/data/access/gbm/ (visited on 06/03/2016).

[9] S Kitamoto et al. "ASTRO-H White Paper-Accreting Pulsars, Magnetars, and Related Sources". In: *arXiv preprint arXiv:1412.1165* (2014).

[10] L Kuiper and W Hermsen. "The soft γ-ray pulsar population: a high-energy overview". In: *Monthly Notices of the Royal Astronomical Society* 449.4 (2015), pp. 3827–3866.

[11] L Kuiper et al. "COMPTEL detection of pulsed gamma-ray emission from PSR B1509-58 up to at least 10 MeV". In: *Astronomy and Astrophysics* 351 (1999), pp. 119–132.

[12] L Kuiper et al. "The Crab pulsar in the 0.75-30 MeV range as seen by CGRO COMPTEL-A coherent high-energy picture from soft X-rays up to high-energy γ-rays". In: *Astronomy & Astrophysics* 378.3 (2001), pp. 918–935.

[13] Samuel K Lander. "The contrasting magnetic fields of superconducting pulsars and magnetars". In: *Monthly Notices of the Royal Astronomical Society* 437.1 (2014), pp. 424–436.

[14] Charles Meegan et al. "The Fermi gamma-ray burst monitor". In: *The Astrophysical Journal* 702.1 (2009), p. 791.

[15] BC Rubin et al. "Observations of 4U 1700-37 with BATSE". In: *The Astrophysical Journal* 459 (1996), p. 259.

[16] Sean G Ryan and Andrew J Norton. *Stellar evolution and nucleosynthesis*. Cambridge University Press, 2010.

[17] B.S. Ryden and B.M. Peterson. *Foundations of Astrophysics*. Pearson, 2011. ISBN: 0321748050.